www.czasopisma.pan.pl PAN POLSKA AKADEMIA NAUK www.journals.pan.pl

PAN ARCHIVES OF ACOUSTICS
Vol. **44**, No. 3, pp. 475–492 (2019)
DOI: 10.24425/aoa.2019.129263

Isogeometric Fast Multipole Boundary Element Method Based on Burton-Miller Formulation for 3D Acoustic Problems

Leilei CHEN(1), Wenchang ZHAO(2), Cheng LIU(2), Haibo CHEN(2), Steffen MARBURG(3)

(1) *College of Architecture and Civil Engineering*
Xinyang Normal University
Xinyang 464000, Henan, P.R.China
*Corresponding Author e-mail: chenllei@mail.ustc.edu.cn

(2) *CAS Key Laboratory of Mechanical Behavior and Design of Materials*
Department of Modern Mechanics
University of Science and Technology of China
Hefei 230026, Anhui, P.R.China

(3) *Institute of Vibroacoustics of Vehicles and Machines*
Faculty of Mechanical Engineering
Technical University of Munich
Boltzmannstr. 15, 85748 Garching bei München, Germany

(*received September 2, 2018; accepted April 2, 2019*)

An isogeometric boundary element method is applied to simulate wave scattering problems governed by the Helmholtz equation. The NURBS (non-uniform rational B-splines) widely used in the CAD (computer aided design) field is applied to represent the geometric model and approximate physical field variables. The Burton-Miller formulation is used to overcome the fictitious frequency problem when using a single Helmholtz boundary integral equation for exterior boundary-value problems. The singular integrals existing in Burton-Miller formulation are evaluated directly and accurately using Hadamard's finite part integration. Fast multipole method is applied to accelerate the solution of the system of equations. It is demonstrated that the isogeometric boundary element method based on NURBS performs better than the conventional approach based on Lagrange basis functions in terms of accuracy, and the use of the fast multipole method both retains the accuracy for isogeometric boundary element method and reduces the computational cost.

Keywords: isogeometric analysis; boundary element method; Burton-Miller method; acoustic scattering; fast multipole method.

1. Introduction

The traditional numerical method divides the geometric model extracted from CAD software into many small grids for numerical integration calculation. For complex practical engineering problems, this step is often the most time-consuming in the whole analysis process. In addition, the geometric error of the analysis model also affects the accuracy of numerical analysis. In order to improve the accuracy, large-scale discretization of the CAD model is often necessary. However, it results in an increase in the amount of calculation and storage. The use of the isogeometric analysis method (IGA) integrates the CAD and CAE (computer aided engineering) models, and realizes the same expression of the geometric and analysis models. No matter how coarse the discretization used for the interpolation calculation of physics field is, the geometric model is always exact, and so the IGA method produces numerical results with higher accuracy than conventional numerical ones based on domain or boundary discretization.

The IGA method in the context of Finite Element Method (FEM) proposed by Hughes *et al.* (2005) uses NURBS widely utilized in the CAD field to represent the geometric model and approximate field variables. Applications of isogeometric Finite Element Method (IGAFEM) include fracture mechan-

ics (De Luycker *et al.*, 2011), electromagnetics field (Takahashi, Matsumoto, 2012; Taus *et al.*, 2016; Zieniuk *et al.*, 2013; Zieniuk, Szerszen, 2014), fluid-structure interaction (Bazilevs *et al.*, 2008; Liu *et al.*, 2018), and so on.

The work presented in this paper focuses on the use of the boundary element method (BEM). As an alternative method to the Finite Element Method and the Finite Difference method, the BEM has several advantages. For example, it can reduce a two dimensional problem down to one dimensional boundary and three dimensional problems down to two dimensional surface. Due to the use of a fundamental solution, the BEM can lead to high accuracies. Especially for the exterior acoustic problems in which we are interested, the Sommerfeld radiation condition is satisfied automatically when BEM is used for numerical solution. The development of isogeometric BEM (IGABEM) is an important research topic, and has attracted the attention of some scholars. The applications of the IGABEM include potential problems (De Luycker *et al.*, 2011), elastostatics (Bai *et al.*, 2015; Bordas *et al.*, 2013; Scott *et al.*, 2013; Simpson *et al.*, 2013), crack problems (Nguyen *et al.*, 2016; Peng *et al.*, 2017a; Peng *et al.*, 2017b), shape optimization (Cho *et al.*, 2009; Kostas *et al.*, 2015; 2017; Lee *et al.*, 2017; Li, Qian, 2011; Lian *et al.*, 2017; Manh *et al.*, 2011; Nguyen *et al.*, 2010; Wall *et al.*, 2008), acoustic problems (Coox *et al.*, 2017; Liu *et al.*, 2017; Peake *et al.*, 2013; 2015; Simpson, Liu, 2016; Simpson *et al.*, 2014), and so on.

When the BEM is applied for the solution of exterior acoustic problems, the non-uniqueness difficulty has to be taken into account because it leads to spurious results. Actually, the CHIEF (the combined Helmholtz integral equation formulation) (Schenck, 1968) and Burton-Miller method (Burton, Miller, 1971) can both be used to overcome this problem. The CHIEF is implemented very easily because it only needs to use some additional collocation points at interior points. However, this method results in an overdetermined system of equations that is difficult to solve. Moreover, it is also difficult to choose some suitable interior points because the exact location and number of additional points are unknown. The Burton-Miller method (BM) combines the conventional and its normal derivative boundary integral equations (Burton, Miller, 1971; Chen *et al.*, 2016a; 2016b; 2017a; 2017b; Marburg *et al.*, 2016; Marburg, Schneider, 2003; Matsumoto *et al.*, 1995; Simpson *et al.*, 2014; Zheng *et al.*, 2015). The disadvantage of this method is difficulty of implementation since hypersingular integrals exist in BM equation. Although BM method has this drawback, it is still used in this work, because of its rigorous mathematical foundation. Simpson *et al.* (2014) presented the derivation process of BM formulation based on IGABEM in 3D acoustic problems, where hypersingular integral is reduced to a weakly singular integral by an appropriate regularization technique. However, the use of Green's function for potential problems decreases the computational efficiency, in particular when the fast multipole method is applied to accelerate the solution of IGABEM. The numerical technique chosen here to evaluate the hypersingular integral was developed by Telles *et al.* (1987), also do Rêgo Silva (1994). Here, the singular integrals can be evaluated directly and accurately by using Hadamard's finite part integration. Actually, in papers (Chen *et al.*, 2017b; Silva *et al.*, 1994; Telles *et al.*, 1987), Lagrange functions are used for the interpolation calculation of physics field, but this work presents the interpolation calculation of physics field based on NURBS basis functions. Some difference is found, such as the expansion expression of interpolation functions and a series of coefficient functions used for the direct evaluation of the hypersingular boundary integral. The derivation process of non-singular BM boundary integral equation based on IGA is presented in detail here.

Another difficulty that is typically encountered in IGABEM is its low computational efficiency because of the non-symmetric and dense coefficient matrix of IGABEM. To improve the computing efficiency of conventional BEM, the fast multipole method (FMM) can be applied to accelerate the operation of matrix-vector for conventional BEM (Coifman *et al.*, 1993; Liu, Nishimura, 2006; Rokhlin *et al.*, 1990; Wolf, Lele, 2011; Zhao *et al.*, 2019). FMM is firstly applied to accelerate the solution of IGABEM for Laplace equation in two dimensions (Takahashi *et al.*, 2012). A black-box FMM is applied for the solution of the three dimensional acoustic IGABEM, where the regularization technique is used for the solution of the hypersingular integrals (Simpson *et al.*, 2016). Hierarchical matrices method is also found to accelerate the solution of IGABEM for elasticity problems (Marussig *et al.*, 2014). In recent years, we have applied FMM for 2D acoustic IGABEM and shaped optimization analysis (Chen *et al.*, 2018; Liu *et al.*, 2017). Actually, there are two different types of FMM, according to expansion form of the Green's function. One is called a low-frequency FMM in which the Green's function is expanded into a multipole form. The other is called diagonal form FMM in which the Green's function is expanded into an exponential form. Actually, both FMMs have some shortcomings. The low-frequency FMM performs inefficiently in high frequencies, and the diagonal form FMM has instability when the computing frequency is very small. The wideband FMM generated by combining the low-frequency FMM and diagonal form FMM can be used successfully to overcome this difficulty (Wofl, Lele, 2011). Herein, the wideband FMM is first applied to accelerate the solution of IGABEM. The series of transfer operations in isogeometric fast multipole boundary element (IGAFMBEM) is presented in this paper, such as Multipole-to-Multipole

(M2M), Multipole-to-Local (M2L) and Local-to-Local (L2L) ones. Finally, several examples are tested to demonstrate the validity and correctness of the algorithm proposed in this paper.

2. NURBS

NURBS are generated from B-splines. Two knot vectors in two dimensions are a set of coordinates in the parametric space, written as $\Xi = [\xi_0, \xi_1, \cdots, \xi_{n+p+1}]$ and $\Upsilon = [\eta_0, \eta_1, \cdots, \eta_{m+l+1}]$, where $\xi_i \in \mathbb{R}$ and $\eta_i \in \mathbb{R}$, i is the knot index, p and l are the polynomial degree, $n+1$ and $m+1$ are the numbers of basis functions.

A control net $\mathbf{P}_{i,j}$ is given to represent the boundary surface, $i = 0, 1, \cdots, n+p+1$ and $j = 0, 1, \cdots, m+l+1$, a tensor product B-spline surface is defined by

$$\mathbf{x}(\xi,\eta) = \sum_{i=0}^{n}\sum_{j=0}^{m} N_{i,p}(\xi)N_{j,l}(\eta)\mathbf{P}_{i,j}, \tag{1}$$

where $\mathbf{x}(\xi,\eta)$ denotes a point on the surface, (ξ,η) means the coordinate in parameter space. $N_{i,p}$ and $N_{j,l}$ are basis functions of B-spline curves. In order to implement the numerical integration in boundary surface based on B-spline, conventional "elements" are taken to be knot spans, namely, $[\xi_i, \xi_{i+1}] * [\eta_j, \eta_{j+1}]$. B-spline is formed by a number of curve segments which can maintain continuity. However, it is difficult for low order B-spline to represent accurately a circle, ellipse, and other complex structures. Using Non-Uniform Rational B-Spline (NURBS), designers can obtain more control of the represented curve without increasing the number of control points or increasing the curve degree. The NURBS basis function and NURBS curve obtained from B-spline are given by

$$R_{i,j}(\xi,\eta) = \frac{N_{i,p}(\xi)N_{j,l}(\eta)w_{i,j}}{W(\xi,\eta)} \tag{2}$$

and

$$\mathbf{x}(\xi,\eta) = \sum_{i=0}^{n}\sum_{j=0}^{m} R_{i,j}(\xi,\eta)\mathbf{P}_{i,j}, \tag{3}$$

where w is the weight, and

$$W(\xi,\eta) = \sum_{a=0}^{n}\sum_{b=0}^{m} N_{a,p}(\xi)N_{b,l}(\eta)w_{a,b}. \tag{4}$$

The sum of rational basis functions $R_{i,j}(\xi,\eta)$ is 1, but we can control the curve by changing the weight of the corresponding control point (basis function). If all weights are equal to 1, the NURBS curve will reduce to a B-spline curve. Actually, in order to implement the numerical integration based on BEM, normal derivative of the boundary surface needs to be solved. By differentiating Eq. (3) with respect to the local coordinate parameter, such as ξ, we can obtain the following formulation:

$$\frac{\partial}{\partial\xi}\mathbf{x}(\xi,\eta) = \sum_{i=0}^{n}\sum_{j=0}^{m}\frac{\partial}{\partial\xi}R_{i,j}(\xi,\eta)\mathbf{P}_{i,j}. \tag{5}$$

By differentiating Eq. (2) with respect to the local coordinate parameter, such as ξ, we can obtain the derivation of the NURBS basis function, as follows:

$$\frac{\partial}{\partial\xi}R_{i,j}(\xi,\eta) = \frac{N'_{i,p}(\xi)N_{j,l}(\eta)w_{i,j} - R_{i,j}(\xi,\eta)W'(\xi,\eta)}{W(\xi,\eta)}, \tag{6}$$

where

$$W'(\xi,\eta) = \sum_{a=0}^{n}\sum_{b=0}^{m} N'_{a,p}(\xi)N_{b,l}(\eta)w_{a,b} \tag{7}$$

and

$$N'_{i,p}(\xi) = \frac{\partial}{\partial\xi}N_{i,p}(\xi). \tag{8}$$

Similarly, we can obtain the derivative of boundary surface with respect to η, as follows:

$$\frac{\partial}{\partial\eta}\mathbf{x} = \sum_{i=0}^{n}\sum_{j=0}^{m}\left(\frac{\partial}{\partial\eta}R_{i,j}(\xi,\eta)\right)\mathbf{P}_{i,j}. \tag{9}$$

Actually, $\frac{\partial}{\partial\xi}\mathbf{x}$ and $\frac{\partial}{\partial\eta}\mathbf{x}$ denote the tangential vector at a point located on the boundary surface, and are simplified to be $\mathbf{V}_\xi$ and $\mathbf{V}_\eta$, respectively. The normal vector at the same point can be obtained from the two tangential vectors, as follows:

$$\mathbf{N} = \mathbf{V}_\xi \times \mathbf{V}_\eta. \tag{10}$$

Finally, we can obtain the unit normal vector, as follows:

$$\mathbf{n} = \mathbf{N}J^{-1}, \tag{11}$$

where

$$J = |\mathbf{N}| = \sqrt{N_1^2 + N_2^2 + N_3^2}. \tag{12}$$

3. IGABEM based on NURBS

For a 3D acoustic problem, the boundary integral equation governed by Helmholtz equation can be written as

$$c(x)p(x) = \int_S G(x,y)q(y)\,\mathrm{d}S(y) - \int_S F(x,y)p(y)\,\mathrm{d}S(y) + p_i(x), \quad x \in \Omega, \tag{13}$$

where $p(x)$ stands for the complex sound pressure, $G(x,y)$ is the Green function, $c(x)$ means the solid angle on the surface, p_i denotes the incident field, and

$q(y)$ and $F(x,y)$ stand for the outward normal derivatives of $p(y)$ and $G(x,y)$ respectively. Herein, we consider the harmonic time dependence $e^{-i\omega t}$. ω denotes the circular frequency.

$$G(x,y) = \frac{e^{\mathbf{i}kr}}{4\pi r} \tag{14}$$

and

$$F(x,y) = \frac{\partial G(x,y)}{\partial n(y)} = -\frac{e^{\mathbf{i}kr}}{4\pi r^2}(1-\mathbf{i}kr)\frac{\partial r}{\partial n(y)}, \tag{15}$$

where $\mathbf{i}$ means the unit imaginary number, k is the wave number, r is the distance between point x and point y. When using Eq. (13) to obtain the pressure on the boundary, the non-uniqueness problem occurs at some fictitious eigen-frequencies. The Burton-Miller method, which is formed by combining Eq. (13) and its derived equation, can be used to overcome this problem, where the coupling parameter α can be chosen as $\mathbf{i}/k$ for $k \geqslant 1$, but $\mathbf{i}$ for $k < 1$. The derivated equation of Eq. (13) can be expressed as

$$c(x)q(x) = \int_S \frac{\partial G(x,y)}{\partial n(x)} q(y)\,\mathrm{d}S(y) - \int_S \frac{\partial F(x,y)}{\partial n(x)} p(y)\,\mathrm{d}S(y) + \frac{\partial p_i(x)}{\partial n(x)}, \tag{16}$$

where

$$\frac{\partial G(x,y)}{\partial n(x)} = -\frac{e^{\mathbf{i}kr}}{4\pi r^2}(1-\mathbf{i}kr)\frac{\partial r}{\partial n(x)} \tag{17}$$

and

$$\frac{\partial F(x,y)}{\partial n(x)} = \frac{e^{\mathbf{i}kr}}{4\pi r^3}\left[(3-3\mathbf{i}kr-k^2r^2)\frac{\partial r}{\partial n(x)}\frac{\partial r}{\partial n(y)} + (1-\mathbf{i}kr)n_i(x)n_i(y)\right]. \tag{18}$$

After discretizing the boundary S, acoustic pressure $p(y)$ in every boundary element can be expressed as

$$p(y) = \sum_{i=1}^{n} \Phi_i p_i. \tag{19}$$

When conventional BEM is used for numerical solution, Φ_i stands for the Lagrange interpolation function. Different types of boundary elements are used to discretize the boundary in (Silva *et al.*, 1994), and the expression of corresponding interpolation functions can be also found in (Silva *et al.*, 1994). When IGA-BEM is used for numerical solution, Φ_i stands for the NURBS basis function.

Actually, when the field point y approaches the source point x, which means the point y lies on the boundary element S_x containing the point x, the boundary integral for the kernel function $G(x,y)$ in Eq. (13) is weakly singular, and the boundary integrals for $F(x,y)$ in Eq. (13) and $\frac{\partial G(x,y)}{\partial n(x)}$ in Eq. (16) are also weakly singular. The weakly singular boundary integrals can be solved accurately by using the polar coordinate transformation (Silva *et al.*, 1994). In the papers by Guiggiani *et al.* (1992) and do Rêgo Silva (1994), Lagrange functions are used for the interpolation calculation of the physics field and geometric surface. Herein, NURBS basis functions are used to represent the boundary surface and approximate the physics field. Due to the difference of the interpolation functions, different expansion expressions for them are obtained, and different expressions for the non-singular boundary integral formulas are also found. In particular, the coefficient functions in the non-singular boundary integral formulas obtained by evaluating the strongly singular boundary integral directly also show different expressions. The corresponding operation procedure for the evaluation of the singular boundary integral based on IGA is presented in Appendices A and B.

4. Isogeometric BEM based on FMM acceleration

In order to decrease the computational time and the memory requirements of the isogeometric BEM proposed in this paper from $O(n^2)$ to $O(n)$ or $O(n\log n)$, the FMM approach is applied to accelerate the matrix-vector product in Eqs (13) and (16). Actually, there are two different types of fast multipole algorithms for acoustic BEM. One is original FMM (also called low-frequency method), and the other is the diagonal form (also called high-frequency method). In this paper, first the fundamentals of the original FMM are presented. However, this method is inefficient for high frequency problems. The diagonal form is introduced to overcome this difficulty. But the diagonal form has an instability problem for the solution of low frequency Helmholtz equations.

Due to the shortcoming of the original FMM and diagonal form FMM at high and low frequencies, respectively, the wideband FMBEM obtained by combining both FMM forms is presented in this paper. The aim of the wideband FMM is to evaluate the far-field boundary integration using the original FMM at low frequency and solve the boundary integration using the diagonal form FMM at high frequency. When the upward pass is implemented, the moments for the original FMM need to be shifted to the moments for the diagonal form FMM with the product (kd^s) increasing, where k is the wave number, and d^s is the edge length of a cell at s level. Similarly, when the down pass is implemented, the local expansion coefficients for the

diagonal form FMM need to be shifted to that for the original FMM with the product (kd^s) decreasing.

The formulation is basically the same as the FMM for the conventional BEM based on Lagrange function interpolation, such as piecewise constant elements, linear elements, quadratic elements. So, it is not necessary to show the entire formulation of the wideband FMM. Herein, we focus on the major differences between isogeometric BEM and conventional BEM with respect to formulation and algorithm of wideband FMM.

4.1. Original FMM formulations for acoustic isogeometric BEM

The FMM relies on the multipole expansion of the Green's function $G(x,y)$ in Eq. (14) to solve the boundary integration when source point x is sufficiently distant form field point y. For 3D problems, the Green's function, i.e., Eq. (14), is expanded into the following series (Coifman *et al.*, 1993; Liu, Nishimura, 2006; Rokhlin *et al.*, 1990; Wolf, Lele, 2011):

$$G(x,y)=\frac{\mathbf{i}k}{4\pi}\sum_{n=0}^{\infty}\sum_{m=-n}^{n}(2n+1)\overline{I}_n^m(k,\mathbf{a_1})O_n^m(k,\mathbf{a_2}), \quad (20)$$

where y_c is an expansion point near y. Vector $\mathbf{a_1}$ represents a directed line segment by y_c pointing to y, and vector $\mathbf{a_2}$ represents a directed line segment by y_c pointing to x. I_n^m and O_n^m are expressed as

$$I_n^m(k,\mathbf{a}) = j_n(kr)Y_n^m(\theta,\phi), \quad (21)$$

$$O_n^m(k,\mathbf{a}) = h_n^{(1)}(kr)Y_n^m(\theta,\phi), \quad (22)$$

and $\overline{I}_n^m$ are the complex conjugates of I_n^m, j_n and $h_n^{(1)}$ are the n-th order spherical Bessel and Hankel functions of the first kind, Y_n^m is the spherical harmonics defined as

$$Y_n^m(\theta,\phi) = c_n^m P_n^m(\cos\theta)\mathrm{e}^{\mathbf{i}m\phi}, \quad (23)$$

where $c_n^m = \sqrt{(n-m)!/(n+m)!}$, P_n^m denotes the associated Legendre functions; r, θ, and ϕ represent the three spherical coordinates of some vector $\mathbf{a}$, such as $\mathbf{a_1}$ or $\mathbf{a_2}$, for instance. S_0 stands for a subset of the boundary S, which is far away from the source point x. Using Eq. (20), we can obtain the Burton-Miller formulation on boundary S_0, as follows:

$$\begin{aligned}A_3 &= \int_{S_0}\left[\left(G(x,y)+\alpha\frac{\partial G(x,y)}{\partial n(x)}\right)q(y)\right.\\ &\quad\left.-\left(F(x,y)+\alpha\frac{\partial F(x,y)}{\partial n(x)}\right)p(y)\right]\mathrm{d}S(y)\\ &= \frac{\mathbf{i}k}{4\pi}\sum_{n=0}^{\infty}\sum_{m=-n}^{n}(2n+1)M_n^m(k,\mathbf{a_1})\\ &\quad\cdot\left[O_n^m(k,\mathbf{a_2})+\alpha\frac{\partial O_n^m(k,\mathbf{a_2})}{\partial n(x)}\right], \end{aligned}\quad (24)$$

where M_n^m is the multipole moment defined by

$$\begin{aligned}M_n^m(k,\mathbf{a_1}) &= \int_{S_0}\overline{I}_n^m(k,\mathbf{a_1})q(y)\,\mathrm{d}S(y)\\ &\quad-\int_{S_0}D_n^m(k,\mathbf{a_1})p(y)\,\mathrm{d}S(y)\\ &= \sum_{i=0}^{n}\sum_{j=0}^{m}\left[\int_{\xi_e}^{\xi_{e+1}}\int_{\eta_e}^{\eta_{e+1}}I_n^m(k,\mathbf{a_1})x^*\right]\mathbf{q}_{i,j}\\ &\quad-\sum_{i=0}^{n}\sum_{j=0}^{m}\left[\int_{\xi_e}^{\xi_{e+1}}\int_{\eta_e}^{\eta_{e+1}}D_n^m(k,\mathbf{a_1})x^*\right]\mathbf{p}_{i,j}, \end{aligned}\quad (25)$$

where

$$x^* = R_{i,j}(\xi,\eta)J(\xi,\eta)\,\mathrm{d}\xi\,\mathrm{d}\eta,$$

and y_c is located close to S_0 and $D_n^m(k,\mathbf{a_1})$ is given by

$$D_n^m(k,\mathbf{a_1}) = \frac{\partial\overline{I}_n^m(k,\mathbf{a_1})}{\partial n(y)}. \quad (26)$$

Actually, computation of the moments depends on the choice of the bases for the geometry y on the boundary surface. However, the remaining computations except for the near-field computation are independent from the choice, such as multipole-to-multipole translation (M2M), multipole-to-local translation (M2L), local-to-local translation (L2L). Hence we can follow Zheng *et al.* (2015) for the successive formulation of the isogeometric fast multipole BEM (IGA-FMBEM) at low frequency.

After the M2M, M2L, and L2L translation operations, A_3 can be expressed as

$$A_3 = \frac{\mathbf{i}k}{4\pi}\sum_{n=0}^{\infty}\sum_{m=-n}^{n}(2n+1)L_n^m(k,x_l^1)\overline{I}_n^m(k,\mathbf{a_3}) \quad (27)$$

where x_l^1 is an expansion point near x, vector $\mathbf{a_3}$ represents a directed line segment by x_l^1 pointing to x, L_n^m is the local expansion coefficient for low-frequency FMM. The detailed information on the M2M, M2L, L2L translation operations and the expression of L_n^m can be found in (Zheng *et al.*, 2015).

4.2. Diagonal formulations for acoustic isogeometric BEM

The plane wave expansion formula of the Green's function (i.e., Eq. (13)) is derived by

$$G(x,y) = \frac{\mathbf{i}k}{16\pi^2}\int_{\overline{S}}\mathrm{e}^{\mathbf{i}k\mathbf{k}\cdot\mathbf{a_4}}T(k,\mathbf{k},\mathbf{a_5})\mathrm{e}^{-\mathbf{i}k\mathbf{k}\cdot\mathbf{a_1}}\,\mathrm{d}\overline{S}, \quad (28)$$

where x_l is an expansion point near x, vector $\mathbf{a_4}$ represents a directed line segment by x_l pointing to x, and vector $\mathbf{a_5}$ represents a directed line segment by y_c pointing to x_l. The integration is taken over the unit

sphere $\bar{S}$, $\mathbf{k}$ denotes the outward unit vector on $\overline{S}$. The diagonal translation function T is expressed as

$$T(k,\mathbf{k},\mathbf{a}) = \sum_{n=0}^{\infty} \mathbf{i}^n (2n+1) h_n^{(1)}(ka) P_n(\mathbf{k}\cdot\mathbf{a}), \tag{29}$$

where P_n stand for the Legendre polynomials.

By substituting Eq. (28) into Eq. (13), we can obtain the formulation on boundary S_0, as follows:

$$A_3 = \frac{\mathbf{i}k}{16\pi^2} \int_{\overline{S}} e^{\mathbf{i}k\mathbf{k}\cdot\mathbf{a_4}} B(k,\mathbf{k},\mathbf{a_1}) T(k,\mathbf{k},\mathbf{a_5})\, \mathrm{d}\overline{S}, \tag{30}$$

where $B(k,\mathbf{k},\mathbf{a_1})$ is the high-frequency moments defined by

$$\begin{aligned} B(k,\mathbf{k},\mathbf{a_1}) &= \int_{S_0} \left[\mathrm{e}^{-\mathbf{i}k\mathbf{k}\cdot\mathbf{a_1}} q(y) - E(\mathbf{a_1}) p(y)\right] \mathrm{d}S(y) \\ &= \sum_{i=0}^{n}\sum_{j=0}^{m} \left[\int_{\xi_e}^{\xi_{e+1}} \int_{\eta_e}^{\eta_{e+1}} \mathrm{e}^{-\mathbf{i}k\mathbf{k}\cdot\mathbf{a_1}} y^*\right] \mathbf{q}_{i,j} \\ &\quad - \sum_{i=0}^{n}\sum_{j=0}^{m} \left[\int_{\xi_e}^{\xi_{e+1}} \int_{\eta_e}^{\eta_{e+1}} E(\mathbf{a_1}) y^*\right] \mathbf{p}_{i,j} \end{aligned} \tag{31}$$

where

$$y^* = R_{i,j}(\xi,\eta) J(\xi,\eta)\, \mathrm{d}\xi\, \mathrm{d}\eta$$

and

$$E(\mathbf{a_1}) = \frac{\partial \mathrm{e}^{-\mathbf{i}k\mathbf{k}\cdot\mathbf{a_1}}}{\partial n(y)}. \tag{32}$$

Similarly, the computation of the moments for high-frequency FMM depends on the choice of the bases for the geometry y on the boundary surface. However, the remaining computations except for the near-field computation are independent from the choice, such as multipole-to-multipole translation (B2B), multipole-to-local translation (B2H), local-to-local translation (H2H). Hence we can also follow Zheng *et al.* (2015) for the successive formulation of the isogeometric fast multipole BEM (IGA-FMBEM) at high frequency.

After the B2B, B2H, H2H translation operations, A_3 can be derived by

$$A_3 = \frac{\mathbf{i}k}{16\pi^2} \int_{\overline{S}} \mathrm{e}^{\mathbf{i}k\mathbf{k}\cdot\mathbf{a_3}} H(k,\mathbf{k},x_l^1)\, \mathrm{d}\overline{S}, \tag{33}$$

where H is the local expansion coefficient for high-frequency FMM. The detailed information on the B2B, B2H, H2H translation operations and the expression of H can be found in (Zheng *et al.*, 2015). It is worth noting that the above expansion expression may cause instability of the diagonal form FMBEM at lower frequencies (Zheng *et al.*, 2012). That is because when the computing frequency is too low, the number of numerical integral points on the unit sphere is too small, resulting in the error of interpolation and filtering used in high-frequency fast algorithm being too large.

4.3. Wideband FMBEM

The wideband FMBEM obtained by combining the original form and the diagonal form of the FMBEM is accurate and efficient. After generating the tree structure, we start the operation of called upward pass, where multipole moments are calculated. When the product (kd^l) is less than a specified number $\overline{v}$ (in this paper, the specified number is set as 0.25), the moments of the original FMM are calculated by M2M translation. Herein, k denotes the wave number, and d^l stands for the edge length of a cell at l level. When $kd^{l+1} > \overline{v}$, the moments of the diagonal form are calculated by B2B translation. When $kd^{l+1} < \overline{v}$ and $kd^l > \overline{v}$, the moments of the original FMM need to be shifted to the moments of the diagonal form by using the M2B formula, as follows:

$$B(k,\mathbf{k},y_c) = \sum_{n=0}^{\infty}\sum_{m=-n}^{n} (2n+1)\, \mathbf{i}^{-n} Y_n^m(\mathbf{k}) M_n^m(k,y_c). \tag{34}$$

After the moments of cells in all levels except for levels 0 and 1 are solved, the downward pass operation will be implemented, in which the local expansion coefficients are calculated. When $kd^l >= \overline{v}$, the local expansion coefficients are calculated by B2H and H2H. When $kd^l < \overline{v}$ and $kd^{l-1} >= \overline{v}$, the local expansion coefficients are calculated by M2L and H2L, where H2L translation can be derived by

$$L_n^m(k,x_l) = \frac{\mathbf{i}^n}{4\pi} \int_{\overline{S}} Y_n^m(\mathbf{k}) H(k,\mathbf{k},x_l)\, \mathrm{d}\overline{S}. \tag{35}$$

On the other hand, we have to truncate the terms used in the functions O, I, M, and L and the number of the plane wave samples along the unit sphere. The number of truncation terms $\overline{z}$ is given in the following form in (Coifman *et al.*, 1993):

$$\overline{z} = kd + \overline{c}\cdot\log(kd+\pi), \tag{36}$$

where $\overline{c}$ is a constant. Actually, the truncation number $\overline{z}$ increases with parameter $\overline{c}$, which leads to an improvement of accuracy but induces a longer computing time and memory usage. Herein, $\overline{c}$ is set as 5 (Coifman *et al.*, 1993).

Using FMM, the coefficient matrices of BEM consist of two parts. One is a near-field part, which is evaluated using standard boundary element techniques. The other is a far-field part, which arises from the series expansion. Applying FMM on a hierarchy of clusters reduces the complexity of BEM from $O(N^2)$ to $O(N\log^2 N)$, where N is the degree of freedom.

5. Numerical examples

In order to verify the validity and correctness of the proposed algorithm, several numerical examples

are presented in this section. First, we consider the acoustic radiation from a sphere with uniform velocity. Figure 1 shows the geometric shape represented by NURBS curve. The second example is considering acoustic scattering from a sphere with a plane incident wave. The third example is considering acoustic scattering from a complex structure. The field outside the sphere is assumed to be air, with the mass density of $\rho = 1.2$ kg/m^3 and the sound speed of $c = 340.0$ m/s.

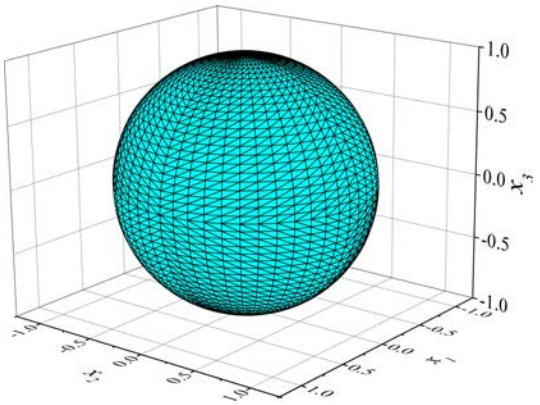

Fig. 1. Pulsating sphere model represented by NURBS curve.

5.1. Pulsating sphere example

In this subsection, the acoustic radiation from a sphere with uniform velocity is considered. The radius of the sphere is 1 m, and the amplitude of the vibrating velocity of the sphere is 1. Figure 2 shows the real and imaginary parts of sound pressure at the computing point located on $(2, 0, 0)$ in terms of frequency, respectively. The iterative solver GMRES terminates the iteration when the residue is below the tolerance 10^{-5}. For IGA-FMBEM, the numbers of discretized elements and collocation points are 1800 and 7082, respectively. For FMBEM, the numbers of discretized elements and collocation points are 1800 and 7082, respectively. From this figure, we can find that the solution by IGA-FMBEM and FMBEM both agree well with the analytical solution, and it demonstrates the validity and correctness of this algorithm proposed in this paper.

Figure 3 shows the real and imaginary parts of acoustic pressure at the computing points distributed on x axis, respectively. We also see that the numerical solution by FMBEM and IGA-FMBEM has a good agreement with the analytical solution. In the Figs 2 and 3, the Burton-Miller formulation is used for the numerical solution.

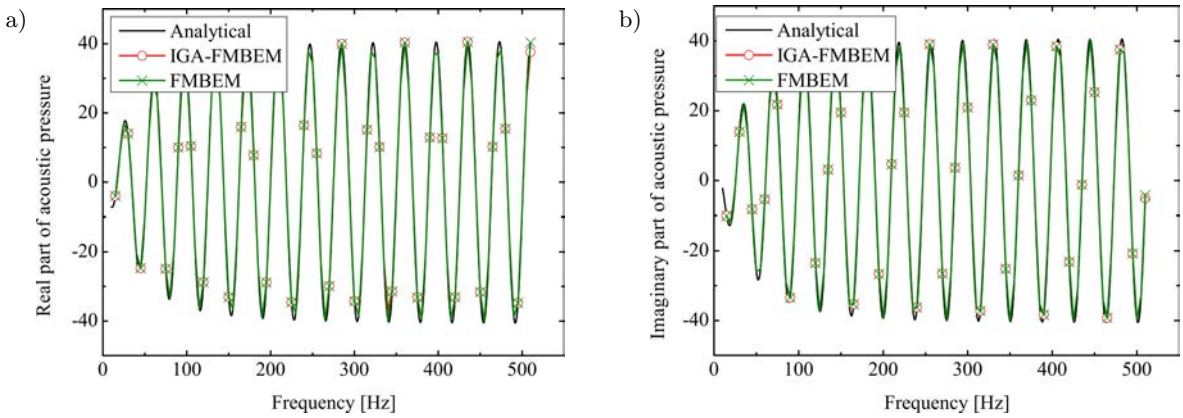

Fig. 2. Real part (a) and imaginary part (b) of sound pressure at the computing point located on $(2, 0, 0)$ in terms of frequency.

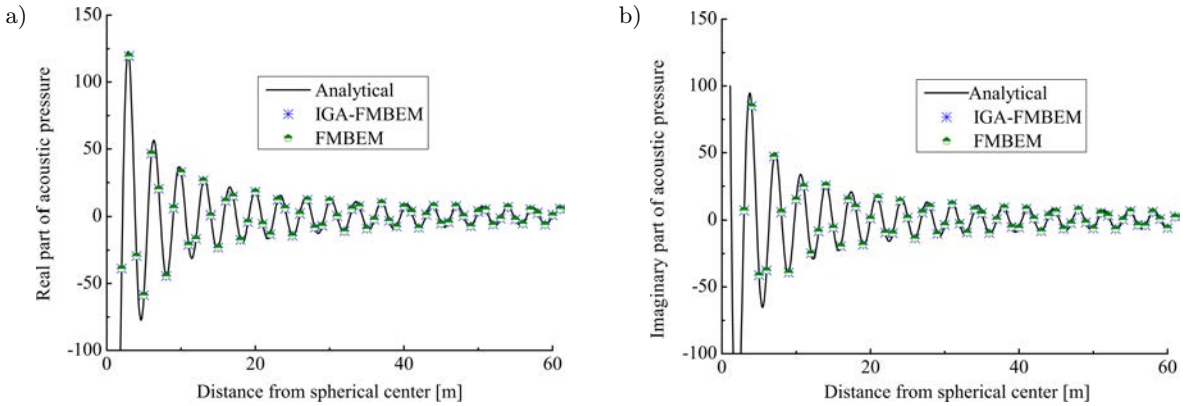

Fig. 3. Real part (a) and imaginary part (b) of acoustic pressure at the computing points distributed on x axis.

In order to compare the computation accuracy of different numerical methods, we define the relative error by

$$\text{error} = \frac{\left|p^{\text{numer}} - p^{\text{analyt}}\right|}{\left|p^{\text{analyt}}\right|}, \tag{37}$$

where p^{numer} denotes the numerical solution of complex sound pressure at a computing point, and p^{analyt} is the analytical result.

Table 1 shows the comparison of the relative error for sound pressure at a point $(2,0,0)$ by NURBS interpolation and conventional Lagrange function interpolation including constant quadrilateral element (BE41), linear discontinuous quadrilateral element with linear geometric approximation (BE44), linear continuous quadrilateral element (CBE44), linear discontinuous quadrilateral element with quadratic geometric approximation (BE94), quadratic continuous quadrilateral element (CBE88), see Fig. 4 or paper (Marburg, Amini, 2005) for more content. In this table, the computing frequency is 100 Hz. There we can see that the solution obtained by Lagrange boundary elements hardly change with the level of Gauss integral quadrature, but the solution obtained by NURBS elements change fast with the level of Gauss integral quadrature, such as 2.19e–5 for 5×5 Gauss-Legendre quadrature and 3.20e–11 for 20×20. Actually, the geometric used for numerical integral is not exact when using Lagrange function interpolation. The deviation between approximated geometric and exact geometric results in a big error of the numerical solution with respect to analytical solution. So, the global error is attributed mainly to the discrete error of geometric approximation. However, when using NURBS discretization, the geometry used for boundary integral is exact, and the global error can be attributed entirely to numerical integration because the solution of the problem is known to be constant over the entire boundary. In addition, we also find that the solution error for 20×20 is below the tolerance for convergence. That is because this example is very special with an extremely simple structural model and boundary condition. In fact, after one iteration, the calculation accuracy can reach about 1.6e–9.

Table 1. Comparison for the computing solution by NURBS interpolation and conventional Lagrange function interpolation with quadrilateral mesh shape.

G-L quadrature	BE41	BE44	CBE44	BE94	CBE88	NURBS
5×5	2.12e–2	3.56e–2	3.84e–2	6.89e–4	2.07e–3	2.19e–5
8×8	2.12e–2	3.57e–2	3.84e–2	6.89e–4	2.07e–3	9.93e–7
10×10	2.12e–2	3.57e–2	3.84e–2	6.89e–4	2.07e–3	1.21e–7
15×15	2.12e–2	3.57e–2	3.84e–2	6.89e–4	2.07e–3	5.23e–10
20×20	2.12e–2	3.57e–2	3.84e–2	6.89e–4	2.07e–3	3.20e–11
NEs	384	96	384	96	96	72
DOFs	384	384	386	384	290	266

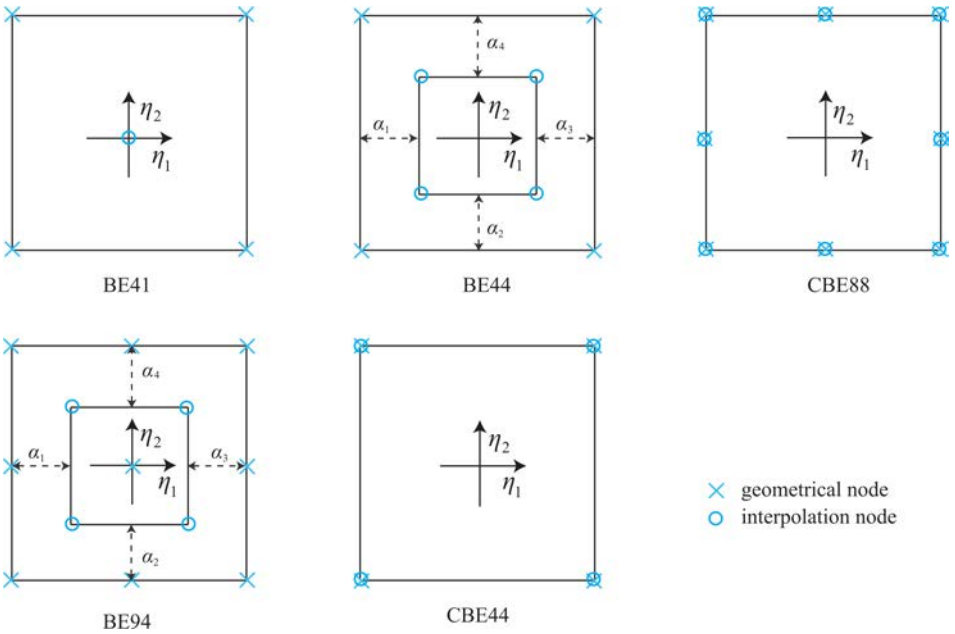

Fig. 4. Distribution of geometrical nodes and interpolation nodes in quadrilateral elements.

Table 2. Comparison for the computing solution by NURBS interpolation and conventional Lagrange function interpolation with triangular mesh shape.

G-L quadrature	BE31	BE33	CBE33	BE63	CBE66	NURBS
5×5	2.67e–2	3.82e–2	4.28e–2	8.56e–3	2.00e–2	2.19e–5
8×8	2.67e–2	3.82e–2	4.28e–2	8.56e–3	2.00e–2	9.93e–7
10×10	2.67e–2	3.82e–2	4.28e–2	8.56e–3	2.00e–2	1.21e–7
15×15	2.67e–2	3.82e–2	4.28e–2	8.56e–3	2.00e–2	5.23e–10
20×20	2.67e–2	3.82e–2	4.28e–2	8.56e–3	2.00e–2	3.20e–11
NEs	432	144	768	144	192	72
DOFs	432	432	384	432	386	266

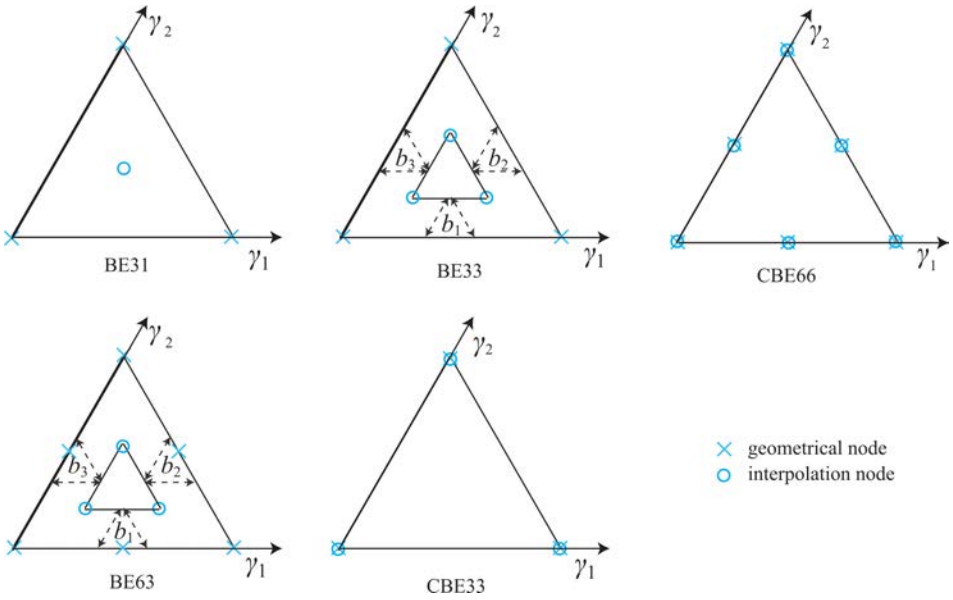

Fig. 5. Distribution of geometrical nodes and interpolation nodes in triangular elements.

Table 2 shows the comparison for the computing solution by NURBS interpolation and conventional Lagrange function interpolation including constant triangular element (BE31), linear discontinuous triangular element with linear geometric approximation (BE33), linear continuous triangular element (CBE33), linear discontinuous triangular element with quadratic geometric approximation (BE63), quadratic continuous triangular element (CBE66), see Fig. 5. Similar as in Table 1, the relative error for the numerical solution obtained by Lagrange discretization is much greater than that obtained by NURBS discretization. Moreover, it demonstrates the validity and correctness of IGA-BEM. In Tables 1 and 2, the CBIE is used for the numerical solution.

We compare the accelerated IGABEM (IGAFMBEM) against an accelerated conventional BEM (FMBEM) in which a GMRES iterative solver is employed with a solver tolerance of 10^{-5} prescribed. All simulations are performed on a 2.4 GHz quadcore processor in which six parallel threads duo to hyperthreading are used for numerical analysis. From this figure, we can find that both methods provide $O(N\log N)$ scaling with the number of DOFs (degrees of freedom). For a similar number of DOFs, the IGAFMBEM runs slowlier than the conventional FMBEM because the NURBS basis functions are obtained by using recursive computation.

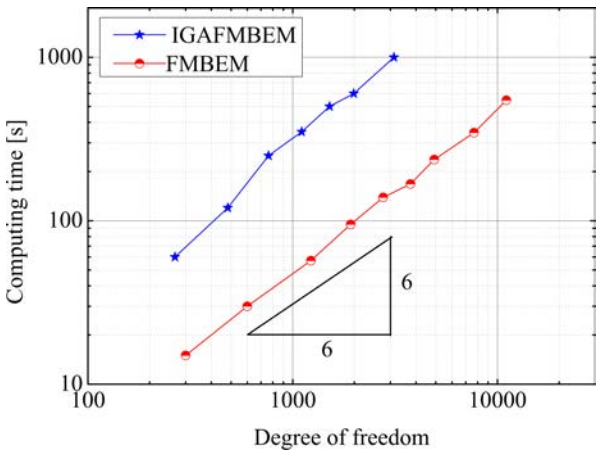

Fig. 6. Comparison of runtimes for the IGAFMBEM and FMBEM applied to a pulsating spherical model.

5.2. Scattering from a sphere

The second example is considering the acoustic scattering of a plane incident wave with a unit amplitude on a sphere with radius $r = 1$ m centered at point $(0, 0, 0)$. The analytical solution for scattering acoustic in the fluid domain can be found in (Zheng *et al.*, 2012). Figure 7 shows the real and imaginary parts of acoustic pressure at a computing point $(10, 0, 0)$ in terms of frequency, respectively. Herein, the numbers of discretized elements and collocation points used for numerical solution are 1800 and 7082, respectively. From this figure, we can see that the solution obtained by IGA-FMBEM-CBIE (IGA-FMBEM based on single boundary integral equation) has a big deviation from the analytical solution at some fictitious eigen-frequencies, such as wave number $k = 3.142$ and $k = 6.283$. Actually, the fictitious eigen-frequencies are the roots of $j_n(kr) = 0$. However, the solution obtained by IGA-FMBEM-BM (IGA-FMBEM based on Burton-Miller method) agrees well with analytical solution at all frequencies.

a)

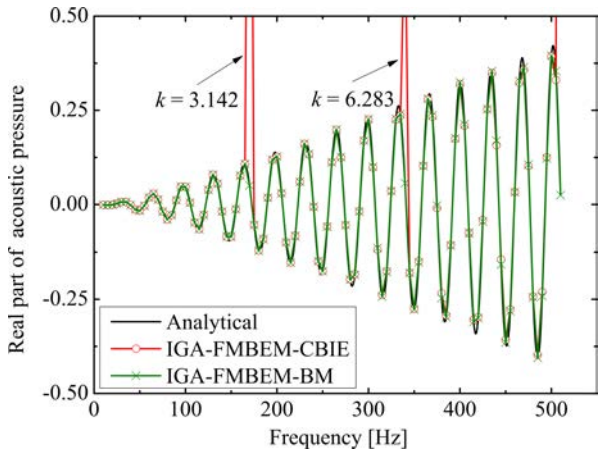

b)

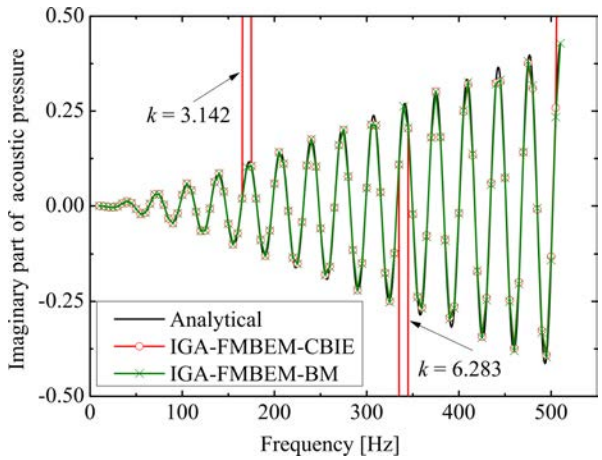

Fig. 7. Real part (a) and imaginary part (b) of acoustic pressure at a computing point $(10, 0, 0)$ in terms of frequency, respectively.

In order to further investigate the accuracy performance of the algorithm proposed in this work, the relative error for the sound pressure amplitude at this computing point in terms of frequencies is given in Fig. 8. Observing the graph, we can find that the solution obtained by using Burton-Miller formulation is basically below 1.e–3. However, the calculation results obtained by using CBIE jump rapidly at some fictitious eigen-frequencies.

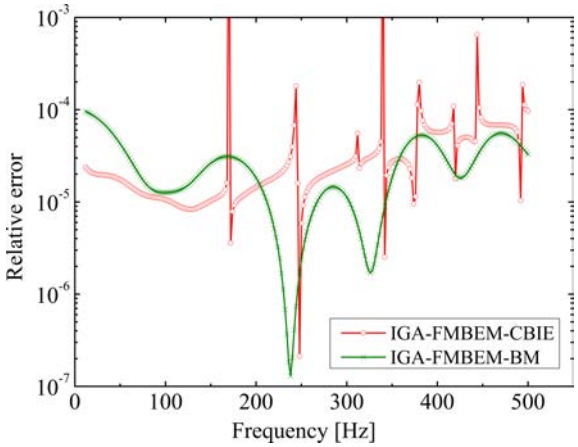

Fig. 8. Relative error for sound pressure amplitude in terms of frequencies.

5.3. Simple submarine model

Numerical simulation of acoustic scattering from large scale shell model is of great significance. For example, by using numerical simulation, we can obtain the acoustic performance and characteristics of submarine, and it will provide the necessary guidance for their acoustic design. More about the vibration radiation of the submarine models can be found in (Merz *et al.*, 2010; Peters *et al.*, 2014). In this subsection, the BeTssi-sub (Benchmark Target Strength Simulation Submarine) model is used to numerical analysis. The bow of the submarine is the semi ellipsoid, the hull is the cylinder, and the stern is the conoid. The size of the submarine structure and the position of coordinate system can be found in Fig. 9, where the origin of coordinate system is located at the major axis of the submarine (also called z axis). When NURBS is used to represent the structural surface, the location

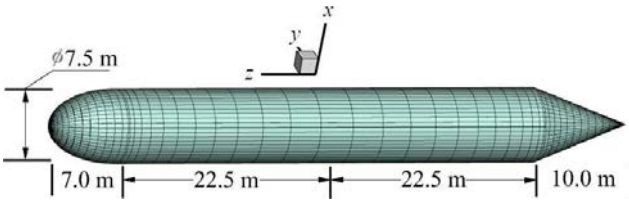

Fig. 9. Simplified physical model of the submarine hull and the position of coordinate system.

of the corresponding control points is given in Fig. 10. The number of collocation points used for interpolation calculation in physics field is set as 8810. The submarine is located in water, and the incident plane wave with a unit amplitude can travel along x axis, y axis, and z axis, respectively.

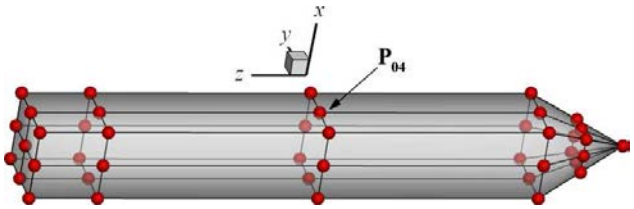

Fig. 10. NURBS control points of the simple BeTSSi; two knot vectors in two dimensions are $\Xi = [0,0,0,0.25,0.25,0.5,0.5,0.75,0.75,1,1,1]$ and $\Upsilon = [0,0,0,0,25,0.25,0.5,0.5,0.75,0.75,1,1,1]$, respectively; the order is $p = 2$ and $l = 2$.

In Figs 11 and 12, the real and imaginary parts contour of acoustic pressure on a square (20×20) m^2 is plotted, respectively, where the square is located on xOy plane and the frequency is 100 Hz. The incident wave is traveling along y axis. From the two figures, we can find that the contour has a strict symmetry along y axis.

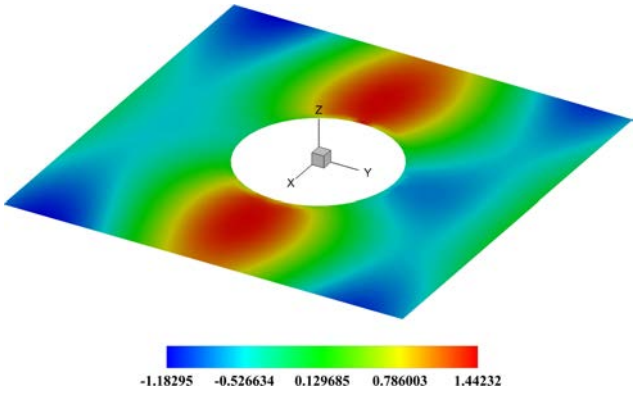

Fig. 11. Real part contour of acoustic pressure on a square located on xOy plane that is perpendicular to the z axis and in which the coordinate of the center point is (0,0,0).

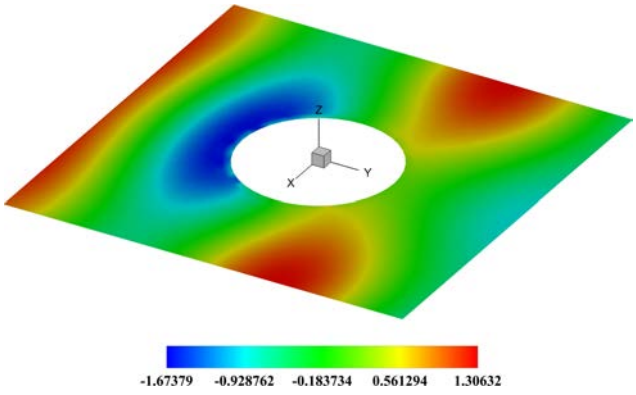

Fig. 12. Imaginary part contour of acoustic pressure on a square located on xOy plane.

Figure 13 shows the comparison of acoustic pressure obtained by FMBEM with that obtained by IGA-FMBEM. "FMBEM" denotes the solution obtained by using the conventional fast multipole BEM, where the element shape is triangular and the DOFs is 93234. The computing points are located on a circle with a radius 6 m on xOy plane. The incident wave is traveling along x axis, and the θ denotes the included angle between the radial direction at a computing point and x axis direction. The figure shows that the solution has a strict symmetry at θ/π, and it denotes that the numerical solution at computing points distributed on a circle has a good symmetry along the incident wave direction (x axis). Moreover, the solution by FMBEM with 93234 DOFs has a good agreement with that by IGA-FMBEM with 14282 DOFs, and it demonstrates the validity and efficiency of IGA for acoustic BEM. Figure 14 shows the comparison of acoustic pressure contour on the surface between the FMBEM and IGA-FMBEM, where the incident wave is traveling along

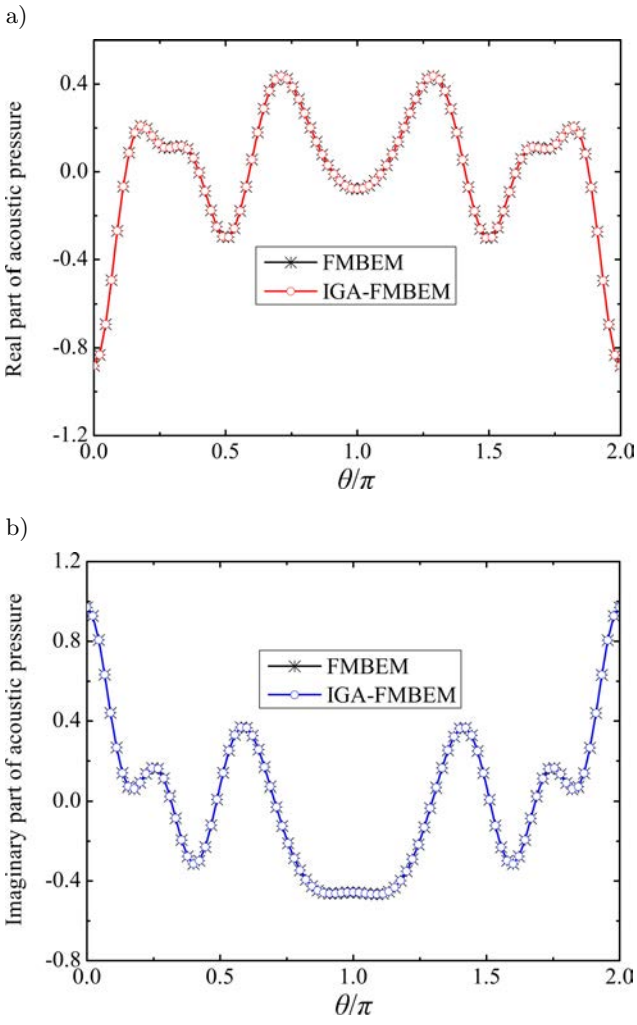

Fig. 13. Real part (a) and imaginary part (b) of acoustic pressure at some computing points located on a circle with a radius 6 m on xOy planes.

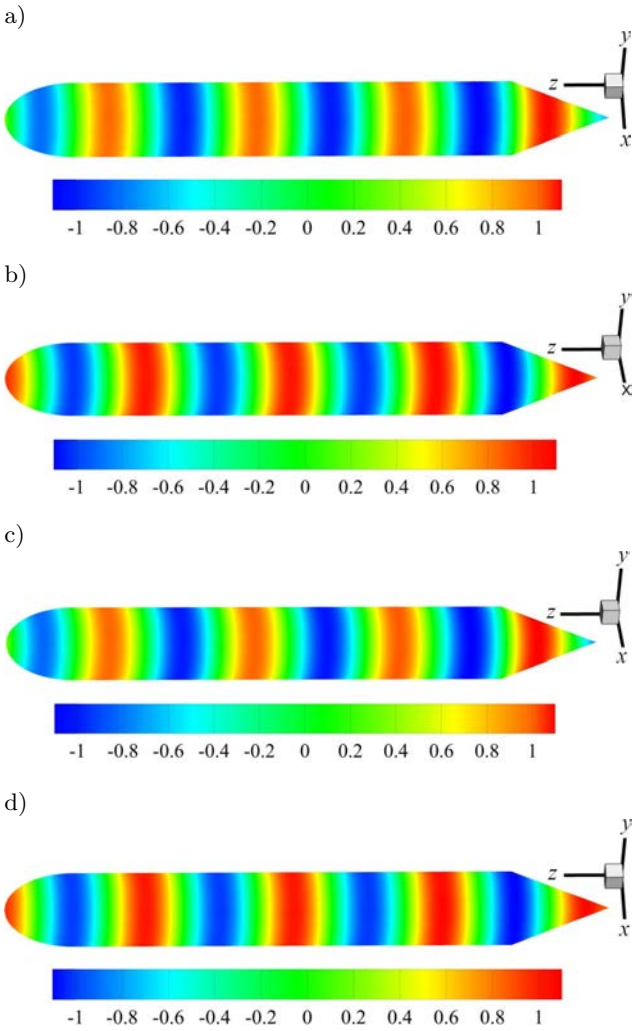

Fig. 14. Contour for real and imaginary parts of acoustic pressure on the structural surface: a) real part of sound pressure with FMBEM, b) imaginary part of sound pressure with FMBEM, c) real part of sound pressure with IGA-FMBEM, d) imaginary part of sound pressure with IGA-FMBEM.

z axis. From this figure, we can find that the solution by FMBEM and IGA-FMBEM both have a good axial symmetry along the incident wave direction, and it keeps good consistency.

6. Conclusion

IGA-FMBEM based on Burton-Miller method is presented for the simulation of 3D acoustic problems, where NURBS basis functions are used to approximate the geometry and physical fields. Hadamard's finite integral method is used to overcome the hypersingular and strong singular boundary integral. The non-singular boundary integral equation based on IGA is presented, and an excellent agreement between the numerical solution obtained by using the algorithm proposed in this paper and analytical solution is observed. By using a pulsating sphere example with analytical solution, we can find that the isogeometric boundary element method presents better results than conventional Lagrange basis functions in terms of accuracy. The expansion approximations in the fast multipole method do not negate the accuracy of the isogeometric boundary element method and so the IGA-FMBEM both retains the IGA accuracy and reduces the computational cost.

Future work will further extend the proposed algorithm into 3D acoustic sensitivity analysis and optimization analysis for practical engineering problems.

Appendix A
Evaluation of weakly singular integral

Firstly, rewriting Eq. (13) as follows:

$$\begin{aligned} c(x)p(x) = &\int\limits_{S-S_x} G(x,y)q(y)\,\mathrm{d}S(y) \\ &- \int\limits_{S-S_x} F(x,y)p(y)\,\mathrm{d}S(y) \\ &+ p_i(x) + A_1 - A_2, \qquad x \in \Omega \end{aligned} \tag{38}$$

where

$$\begin{aligned} A_1 &= \int\limits_{S_x} G(x,y)q(y)\,\mathrm{d}S(y), \\ A_2 &= \int\limits_{S_x} F(x,y)p(y)\,\mathrm{d}S(y). \end{aligned} \tag{39}$$

By substituting Eq. (19) into Eq. (39), we can obtain the following

$$\begin{aligned} A_1 &= \sum_{i=0}^{n}\sum_{j=0}^{m}\left[\int\limits_{\xi_e}^{\xi_{e+1}}\int\limits_{\eta_e}^{\eta_{e+1}} G(x,y)z^*\right]\mathbf{q}_{i,j}, \\ A_2 &= \sum_{i=0}^{n}\sum_{j=0}^{m}\left[\int\limits_{\xi_e}^{\xi_{e+1}}\int\limits_{\eta_e}^{\eta_{e+1}} F(x,y)z^*\right]\mathbf{p}_{i,j}, \end{aligned} \tag{40}$$

where

$$z^* = R_{i,j}(\xi,\eta)J(\xi,\eta)\,\mathrm{d}\xi\,\mathrm{d}\eta,$$

$[\xi_e,\xi_{e+1}]\times[\eta_e,\eta_{e+1}]$ denotes the location space taken by the boundary element S_x. And then, building a polar coordinate system centered at source point x, the relation between the polar coordinate and local parameter coordinate can be expressed as

$$\begin{aligned} \xi &= \xi_x + \rho\cos(\theta), \\ \eta &= \eta_x + \rho\sin(\theta), \end{aligned} \tag{41}$$

where (ξ_x, η_x) stands for the parameter coordinate of the source point x, ρ, and θ are the radial and angular coordinates of the polar coordinate system, respectively. By substituting Eq. (41) into Eq. (40), we can obtain the following expression:

$$A_1 = \sum_{i=0}^{n}\sum_{j=0}^{m}\left[\int_0^{2\pi}\int_0^{\rho(\theta)} GR_{i,j}J\rho\,\mathrm{d}\rho\,\mathrm{d}\theta\right]\mathbf{q}_{i,j},$$
$$A_2 = \sum_{i=0}^{n}\sum_{j=0}^{m}\left[\int_0^{2\pi}\int_0^{\rho(\theta)} FR_{i,j}J\rho\,\mathrm{d}\rho\,\mathrm{d}\theta\right]\mathbf{p}_{i,j}. \tag{42}$$

These integrals in the above equation are solvable because the Jacobian of the coordinate transformation (ρ) cancels out the $1/r$ weak singularity. Solving the boundary integral for quadratic boundary element in Eq. (42) directly is unnecessary, a comfortable alternative method is to subdivide the quadratic element into four triangular elements and then solve the boundary integrals at every triangular element in a simple way, see Fig. 15 or (Silva *et al.*, 1994). Then, Eqs (42) can be expressed as

$$A_1 = \sum_{i=0}^{n}\sum_{j=0}^{m}\sum_{k=1}^{4}\left[\int_{\theta_1}^{\theta_2}\int_0^{\rho(\theta)} GR_{i,j}J\rho\,\mathrm{d}\rho\,\mathrm{d}\theta\right]\mathbf{q}_{i,j},$$
$$A_2 = \sum_{i=0}^{n}\sum_{j=0}^{m}\sum_{k=1}^{4}\left[\int_{\theta_1}^{\theta_2}\int_0^{\rho(\theta)} FR_{i,j}J\rho\,\mathrm{d}\rho\,\mathrm{d}\theta\right]\mathbf{p}_{i,j}, \tag{43}$$

where θ_1 and θ_2 denote the polar coordinate angles of two sides passing through the collocation point (node) in a triangular element. The weak singular boundary integrals showed in Eq. (43) are allowed to be solved directly by using Gauss integral rule.

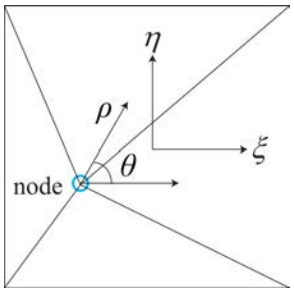

Fig. 15. Subdivision of a quadratic element into four triangular elements.

Appendix B
Evaluation of hypersingular integral

When the Burton-Miller method is used for numerical solution of IGABEM, the boundary integral for $\frac{\partial F(x,y)}{\partial n(x)}$ function is hypersingular. It is still difficult to eliminate the hypersingularity by using polar coordinate translation because this method can only decrease the first order singularity. However, Hadamard's finite integral method can be used to overcome this difficulty, although the implementation procedure of this method is complex. The boundary integral formulas for $\frac{\partial F(x,y)}{\partial n(x)}$ function when y point approaches point x can be rewritten as

$$\int_{S_x}\frac{\partial F(x,y)}{\partial n(x)}p(y)\,\mathrm{d}S(y) = \lim_{\varepsilon\to 0}\int_{S_x-e_\varepsilon}\frac{\partial F(x,y)}{\partial n(x)}p(y)\,\mathrm{d}S(y) + \lim_{\varepsilon\to 0}\int_{S_\varepsilon}\frac{\partial F(x,y)}{\partial n(x)}p(y)\,\mathrm{d}S(y), \tag{44}$$

where S_ε stands for a half spherical surface centered in point x with a radius ε, and e_ε stands for a circle centered in point x with a radius ε. The first limit integral in Eq. (44) is marked as B_1. First, we solve the second limit integral in Eq. (44). On S_ε, the following formulas are valid:

$$\lim_{\varepsilon\to 0}\frac{\partial r}{\partial n(y)} = 1, \tag{45}$$

$$\lim_{\varepsilon\to 0}\frac{\partial r}{\partial n(x)} = -\lim_{\varepsilon\to} n_l(x)n_l(y). \tag{46}$$

Using the above two equations, we can rewrite the second limit integral in Eq. (44) as

$$-\frac{1}{2\pi}\lim_{\varepsilon\to 0}\int_0^{\pi}\frac{n_l(x)n_l(y)}{\varepsilon}p(x)\,\mathrm{d}\theta = -\frac{1}{2\pi}\sum_{i=0}^{n}\sum_{j=0}^{m}\lim_{\varepsilon\to 0}\int_0^{\pi}\frac{n_l(x)n_l(y)}{\varepsilon}R_{i,j}(\xi_x,\eta_x)\mathbf{p}_{i,j}\,\mathrm{d}\theta. \tag{47}$$

B_1 can be rewritten as the following formulas using Eq. (19)

$$B_1 = \sum_{i=0}^{n}\sum_{j=0}^{m}B_{i,j}\mathbf{p}_{i,j}, \tag{48}$$

where

$$B_{i,j} = \lim_{\varepsilon\to 0}\left\{\int_{\xi_e}^{\xi_{e+1}}\int_{\eta_e}^{\eta_{e+1}}\frac{\partial F(x,y)}{\partial n(x)}R_{i,j}(\xi_y,\eta_y)J(\xi_y,\eta_y)\,\mathrm{d}\xi\,\mathrm{d}\eta\right\}. \tag{49}$$

Obviously, function $B_{i,j}$ is hypersingular when point y approaches point x. The key point is to solve $B_{i,j}$ accurately. Using the polar coordinate system to replace the local parameter system shown in Eq. (49), we can obtain the following formulas:

$$B_{i,j} = \lim_{\varepsilon\to 0}\left\{\int_0^{2\pi}\int_{\rho_1}^{\rho_2}W(\rho,\theta)\,\mathrm{d}\rho\,\mathrm{d}\theta\right\}, \tag{50}$$

where ρ_1 is equal to ϵ, ρ_2 is a function of angle θ, and stands for the distance between the collocation point (the central point of the polar coordinate system) and the point with θ angle on the boundary of the quadrilateral element

$$W(\rho,\theta) = \frac{\partial F(x,y)}{\partial n(x)} R_{i,j}(\xi_y,\eta_y) J(\xi_y,\eta_y)\rho. \tag{51}$$

We can find that the highest singular term in kernel function $\frac{\partial F(x,y)}{\partial n(x)}$ is $n_l(x)n_l(y)/4\pi r^3$ when r is very small. By using polar coordinate translation, the formulas for the highest singular term can be rewritten as

$$f(\rho,\theta) = \frac{n_l(x)n_l(y)}{4\pi r^3} R_{i,j}(\xi_y,\eta_y) J(\xi_y,\eta_y)\rho. \tag{52}$$

When ρ is very small, $f(\rho,\theta)$ can be expanded into the following form:

$$f(\rho,\theta) = \frac{f_2(\theta)}{\rho^2} + \frac{f_1(\theta)}{\rho} + \frac{f_0(\theta)}{\rho^0}, \tag{53}$$

where the derivations for $f_1(\theta)$and $f_2(\theta)$ can be found in the Appendix A. Obviously, the singular terms in $W(\rho,\theta)$ are $\frac{f_2(\theta)}{\rho^2}$ and $\frac{f_1(\theta)}{\rho}$. When we eliminate the two singular terms, we can obtain the non-singular expression, and then we can obtain the new expression of $B_{i,j}$, as follows:

$$\begin{aligned} B_{i,j} = &\lim_{\varepsilon\to 0}\left\{\int_0^{2\pi}\int_{\rho_1}^{\rho_2}\left[W(\rho,\theta) - \left(\frac{f_2(\theta)}{\rho^2} + \frac{f_1(\theta)}{\rho}\right)\right]\mathrm{d}\rho\,\mathrm{d}\theta\right\} \\ &+ \lim_{\varepsilon\to 0}\left\{\int_0^{2\pi}\int_{\rho_1}^{\rho_2}\frac{f_1(\theta)}{\rho}\,\mathrm{d}\rho\,\mathrm{d}\theta\right\} \\ &+ \lim_{\varepsilon\to 0}\left\{\int_0^{2\pi}\int_{\rho_1}^{\rho_2}\frac{f_2(\theta)}{\rho^2}\,\mathrm{d}\rho\,\mathrm{d}\theta\right\}, \end{aligned} \tag{54}$$

where ρ_1 is very small. It can be found that the first term on the right hand of Eq. (54) is non-singular, and can be expressed as the following formulation by subdividing the quadratic element into four triangular elements:

$$\sum_{k=1}^{4}\lim_{\varepsilon\to 0}\int_{\theta_1}^{\theta_2}\int_{\rho_1}^{\rho_2(\theta)}\left[W(\rho,\theta) - \left(\frac{f_2(\theta)}{\rho^2} + \frac{f_1(\theta)}{\rho}\right)\right]\mathrm{d}\rho\,\mathrm{d}\theta, \tag{55}$$

where integration in the above equation can be solved directly by using Gauss integral method.

The second term on the right hand of Eq. (54) marked as I_1 and the third one marked as I_2 are both singular, and need to be treated specially. Firstly, by using Taylor expansion, $\rho_1(\varepsilon,\theta)$ can be expressed as

$$\rho_1 = \varepsilon\beta(\theta) + \varepsilon^2\gamma(\theta) + O(\varepsilon^3). \tag{56}$$

We rewrite I_1 as

$$I_1 = \int_0^{2\pi} f_1(\theta)\left(\lim_{\varepsilon\to 0}\int_{\rho_1}^{\rho_2(\theta)}\frac{\mathrm{d}\rho}{\rho}\right)\mathrm{d}\theta. \tag{57}$$

Using Eq. (56) and omitting high-order minor terms, the limit integral in brackets in the above equation can be derived by

$$\begin{aligned} \lim_{\varepsilon\to 0}\int_{\rho_1}^{\rho_2(\theta)}\frac{\mathrm{d}\rho}{\rho} &= \ln\rho_2(\theta) - \lim_{\varepsilon\to 0}\ln\rho_1 \\ &= \ln\frac{\rho_2(\theta)}{\beta(\theta)} - \lim_{\varepsilon\to 0}\ln\varepsilon. \end{aligned} \tag{58}$$

And then, substituting Eq. (58) into Eq. (57), we can obtain the following expression:

$$I_1 = \int_0^{2\pi} f_1(\theta)\ln\left|\frac{\rho_2(\theta)}{\beta(\theta)}\right|\mathrm{d}\theta - \lim_{\varepsilon\to 0}\left[\ln\varepsilon\int_0^{2\pi} f_1(\theta)\,\mathrm{d}\theta\right]. \tag{59}$$

In order to meet Lipschitz condition, the solution of $\int_0^{2\pi} f_1(\theta)\,\mathrm{d}\theta$ must be equal to zero. So, I_1 can be expressed as

$$I_1 = \int_0^{2\pi} f_1(\theta)\ln\left|\frac{\rho_2(\theta)}{\beta(\theta)}\right|\mathrm{d}\theta. \tag{60}$$

Subsequently, we still need to solve I_2. We rewrite I_2 as

$$I_2 = \int_0^{2\pi} f_2(\theta)\left(\lim_{\varepsilon\to 0}\int_{\rho_1}^{\rho_2(\theta)}\frac{\mathrm{d}\rho}{\rho^2}\right)\mathrm{d}\theta. \tag{61}$$

The limit integral in brackets in the above equation can be derived by

$$\lim_{\varepsilon\to 0}\int_{\rho_1}^{\rho_2(\theta)}\frac{\mathrm{d}\rho}{\rho^2} = -\frac{1}{\rho_2(\theta)} + \lim_{\varepsilon\to 0}\frac{1}{\rho_1(\theta)}. \tag{62}$$

We need to obtain the expansion expression of $\frac{1}{\rho_1(\theta)}$. Actually, ε is also a function of ρ_1, and can be expanded as

$$\varepsilon = \overline{\beta}\rho_1 + \overline{\gamma}\rho_1^2 + O(\rho_1^3). \tag{63}$$

And then, substituting Eq. (56) into Eq. (63), we can obtain the expression of $\overline{\beta}$ and $\overline{\gamma}$, as follows:

$$\overline{\beta} = \frac{1}{\beta(\theta)}, \qquad \overline{\gamma} = \frac{-\gamma(\theta)}{\beta^3(\theta)}. \tag{64}$$

Rewriting Eq. (63), we can obtain the expression of $\frac{1}{\rho_1(\theta)}$, as follows:

$$\frac{1}{\rho_1(\theta)} = \frac{1}{\varepsilon\beta(\theta)} - \frac{\gamma(\theta)}{\beta^2(\theta)}. \tag{65}$$

By substituting Eqs (65) and (62) into Eq. (61), we can obtain the new expression, as follows:

$$I_2 = -\int_0^{2\pi} f_2(\theta)\left[\frac{\gamma(\theta)}{\beta^2(\theta)}+\frac{1}{\rho_2(\theta)}\right]\mathrm{d}\theta + \lim_{\varepsilon\to 0}\left[\frac{1}{\varepsilon}\int_0^{2\pi}\frac{f_2(\theta)}{\beta(\theta)}\,\mathrm{d}\theta\right]. \tag{66}$$

Obviously, the solution of the second term on the right hand of Eq. (66) is infinite. By substituting Eqs (60) and (66) into (54), we can obtain new expression of $B_{i,j}$, as follows:

$$\begin{aligned} B_{i,j} = {} & \int_0^{2\pi}\int_0^{\rho_2}\left[W(\rho,\theta)-\left(\frac{f_2(\theta)}{\rho^2}+\frac{f_1(\theta)}{\rho}\right)\right]\mathrm{d}\rho\,\mathrm{d}\theta \\ & + \int_0^{2\pi} f_1(\theta)\ln\left|\frac{\rho_2(\theta)}{\beta(\theta)}\right|\mathrm{d}\theta \\ & - \int_0^{2\pi} f_2(\theta)\left[\frac{\gamma(\theta)}{\beta^2(\theta)}+\frac{1}{\rho_2(\theta)}\right]\mathrm{d}\theta \\ & + \lim_{\varepsilon\to 0}\left[\frac{1}{\varepsilon}\int_0^{2\pi}\frac{f_2(\theta)}{\beta(\theta)}\,\mathrm{d}\theta\right]. \end{aligned} \tag{67}$$

By substituting the above equation into Eq. (48), we can obtain new expression of B_1, as follows:

$$\begin{aligned} B_1 = {} & \sum_{i=0}^{n}\sum_{j=0}^{m}\int_0^{2\pi}\int_0^{\rho_2}\left[W(\rho,\theta)-\left(\frac{f_2(\theta)}{\rho^2}+\frac{f_1(\theta)}{\rho}\right)\right]\mathrm{d}\rho\,\mathrm{d}\theta\mathbf{p}_{i,j} \\ & + \sum_{i=0}^{n}\sum_{j=0}^{m}\int_0^{2\pi} f_1(\theta)\ln\left|\frac{\rho_2(\theta)}{\beta(\theta)}\right|\mathrm{d}\theta\mathbf{p}_{i,j} \\ & - \sum_{i=0}^{n}\sum_{j=0}^{m}\int_0^{2\pi} f_2(\theta)\left[\frac{\gamma(\theta)}{\beta^2(\theta)}+\frac{1}{\rho_2(\theta)}\right]\mathrm{d}\theta\mathbf{p}_{i,j} \\ & + \sum_{i=0}^{n}\sum_{j=0}^{m}\lim_{\varepsilon\to 0}\left[\frac{1}{\varepsilon}\int_0^{2\pi}\frac{f_2(\theta)}{\beta(\theta)}\,\mathrm{d}\theta\right]\mathbf{p}_{i,j}. \end{aligned} \tag{68}$$

According to Lyapunow-Tauber theory (Kupradze, 1965), in order to meet the requirements of smooth continuity, the last term on the right hand of Eq. (68) and the second limit integral in Eq. (44) must cancel each other. So, the non-singular boundary integral formulas for $\frac{\partial F(x,y)}{\partial n(x)}$ function when point y approaches point x can be expressed as

$$\begin{aligned} & \int_{S_x}\frac{\partial F(x,y)}{\partial n(x)}p(y)\,\mathrm{d}S(y) \\ & = \sum_{i=0}^{n}\sum_{j=0}^{m}\int_0^{2\pi}\int_0^{\rho_2}\left[W(\rho,\theta)-\left(\frac{f_2(\theta)}{\rho^2}+\frac{f_1(\theta)}{\rho}\right)\right]\mathrm{d}\rho\,\mathrm{d}\theta\mathbf{p}_{i,j} \\ & \quad + \sum_{i=0}^{n}\sum_{j=0}^{m}\int_0^{2\pi} f_1(\theta)\ln\left|\frac{\rho_2(\theta)}{\beta(\theta)}\right|\mathrm{d}\theta\mathbf{p}_{i,j} \\ & \quad - \sum_{i=0}^{n}\sum_{j=0}^{m}\int_0^{2\pi} f_2(\theta)\left[\frac{\gamma(\theta)}{\beta^2(\theta)}+\frac{1}{\rho_2(\theta)}\right]\mathrm{d}\theta\mathbf{p}_{i,j}, \end{aligned} \tag{69}$$

where the coefficients $f_1(\theta)$, $f_2(\theta)$, $\beta(\theta)$, and $\gamma(\theta)$ are obtained using Taylor's expansion, see Appendix C. After we obtain the expression of all the coefficient functions, we can obtain the non-singular BM formulation. Although the expression of Eq. (69) in form is consistent with that in the literature (Silva *et al.*, 1994; Telles *et al.*, 1987), these coefficient functions have different expression because of the use of different interpolation functions.

Appendix C
Evaluation of coefficient functions

First, we try to get the expressions of $\beta(\theta)$ and $\gamma(\theta)$. By using Taylor's expansion, $y_i - x_i$ in polar coordinate system this can be expressed as

$$y_i - x_i = \rho A_i(\theta) + \rho^2 B_i(\theta) + O(\rho^3), \tag{70}$$

where

$$A_i(\theta) = \cos(\theta)\frac{\partial x_i}{\partial \xi}\bigg|_{\xi_x,\eta_x} + \sin(\theta)\frac{\partial x_i}{\partial \eta}\bigg|_{\xi_x,\eta_x} \tag{71}$$

and

$$\begin{aligned} B_i(\theta) = {} & \frac{\cos^2(\theta)}{2}\frac{\partial^2 x_i}{\partial \xi^2}\bigg|_{\xi_x,\eta_x} + \cos(\theta)\sin(\theta)\frac{\partial^2 x_i}{\partial \xi\partial \eta}\bigg|_{\xi_x,\eta_x} \\ & + \frac{\sin^2(\theta)}{2}\frac{\partial^2 x_i}{\partial \eta^2}\bigg|_{\xi_x,\eta_x}. \end{aligned} \tag{72}$$

By using Taylor's expansion for $r = |y - x|$, we can obtain the expression of n-th power of r, as follows:

$$r^n = \rho^n A^n(\theta)\left[1 + n\rho\frac{A_k(\theta)B_k(\theta)}{A^2(\theta)}\right] + O(\rho^{n+2}), \tag{73}$$

where

$$A(\theta) = \left[A_1^2(\theta) + A_2^2(\theta) + A_3^2(\theta)\right]^{1/2}, \tag{74}$$

$$B(\theta) = \left[B_1^2(\theta) + B_2^2(\theta) + B_3^2(\theta)\right]^{1/2}. \tag{75}$$

By setting $n = 1$ and $r = \varepsilon$ in Eq. (73), we can obtain the expansion of ε, as follows:

$$\varepsilon = \rho_1 A(\theta) + \rho_1^2 \frac{A_k(\theta)B_k(\theta)}{A(\theta)} + O(\rho_1^3), \tag{76}$$

where ρ_1 denotes the value of ρ when field point y on $S_x - e_\varepsilon$ is close to e_ε. And then, by substituting Eq. (56) into Eq. (76), we can obtain the expression of $\beta(\theta)$ and $\gamma(\theta)$, as follows:

$$\beta(\theta) = A^{-1}(\theta), \tag{77}$$

$$\gamma(\theta) = -\frac{A_k(\theta)B_k(\theta)}{A^4(\theta)}. \tag{78}$$

By setting $n = -3$ in Eq. (73), we can obtain the expansion of r^{-3}, as follows:

$$\frac{1}{r^3} = \frac{S_3(\theta)}{\rho^3} + \frac{S_2(\theta)}{\rho^2} + O\left(\frac{1}{\rho}\right), \tag{79}$$

where

$$S_3(\theta) = A^{-3}(\theta), \tag{80}$$

$$S_2(\theta) = -\frac{3A_k(\theta)B_k(\theta)}{A^5(\theta)}. \tag{81}$$

And then, by using Taylor's expansion for NURBS basis function $R_{i,j}(\xi_y, \eta_y)$, we can obtain the following formulas, in which the expansion point is source point x:

$$\begin{aligned} R_{i,j}(\xi_y, \eta_y) &= R_{i,j}(\xi_x, \eta_x) + \rho\left[\cos(\theta)\frac{\partial R_{i,j}}{\partial \xi}\bigg|_{\xi_x,\eta_x}\right. \\ &\quad \left. + \sin(\theta)\frac{\partial R_{i,j}}{\partial \eta}\bigg|_{\xi_x,\eta_x}\right] + O(\rho^2) \\ &= R^0_{i,j} + \rho R^1_{i,j} + O(\rho^2). \end{aligned} \tag{82}$$

The remaining term $n_l(x)n_l(y)J(\xi_y, \eta_y)$ in Eq. (52) also needs to be expanded. First, by using local parameter system, we can rewrite this term into the following formulation

$$\begin{aligned} n_l(x)n_l(y)J(\xi_y, \eta_y) &= n_l(\xi_x, \eta_x)n_l(\xi_y, \eta_y)J(\xi_y, \eta_y) \\ &= n_l(\xi_x, \eta_x)J_l(\xi_y, \eta_y). \end{aligned} \tag{83}$$

And then, by using Taylor's expansion for this term, we can obtain its new expression, in which the expansion point is source point (ξ_x, η_x)

$$\begin{aligned} n_l(\xi_x, \eta_x)J_l(\xi_y, \eta_y) &= n_l(\xi_x, \eta_x)J_l(\xi_x, \eta_x) \\ +\rho n_l(\xi_x, \eta_x)&\left[\cos(\theta)\frac{\partial J_l}{\partial \xi}\bigg|_{\xi_x,\eta_x} + \sin(\theta)\frac{\partial J_l}{\partial \eta}\bigg|_{\xi_x,\eta_y}\right] + O(\rho^2) \\ &= J(\xi_x, \eta_x) + \rho n_l(\xi_x, \eta_x)J^1_l(\xi_x, \eta_x) + O(\rho^2) \\ &= J_0 + \rho J_{01} + O(\rho^2). \end{aligned} \tag{84}$$

By substituting Eqs (84), (83), (82), and (79) into Eq. (52), we can obtain the following formulas:

$$\begin{aligned} f(\rho, \theta) &= \frac{\rho}{4\pi}\left(\frac{S_3(\theta)}{\rho^3} + \frac{S_2(\theta)}{\rho^2} + O\left(\frac{1}{\rho}\right)\right) \\ &\quad \cdot \left(R^0_{i,j} + \rho R^1_{i,j} + O(\rho^2)\right)\left(J_0 + \rho J_{01} + O(\rho^2)\right) \\ &= \frac{S_3 R^0_{i,j} J_0}{4\pi\rho^2} + \frac{S_2 R^0_{i,j} J_0 + S_3\left(R^1_{i,j} J_0 + R^0_{i,j} J_{01}\right)}{4\pi\rho} + O(\rho^0). \end{aligned} \tag{85}$$

Finally, by substituting Eq. (85) into Eq. (53), we can obtain the expression of coefficient $f_1(\theta)$ and $f_2(\theta)$, as follows:

$$f_1(\theta) = \frac{S_2 R^0_{i,j} J_0 + S_3\left(R^1_{i,j} J_0 + R^0_{i,j} J_{01}\right)}{4\pi} \tag{86}$$

and

$$f_2(\theta) = \frac{S_3 R^0_{i,j} J_0}{4\pi}. \tag{87}$$

Acknowledgements

This study was funded by the National Natural Science Foundation of China (NSFC) under Grant no. 11702238 and no. 11772322, Henan Provincial Department of Science and Technology Research under Grant no. 172102210453, Key Scientific Research Project of Henan University under Grant no. 17A560009, and Nanhu Scholars Program for Young Scholars of XYNU.

References

1. Bai Y., Dong C. Y., Liu Z.Y. (2015), *Effective elastic properties and stress states of doubly periodic array of inclusions with complex shapes by isogeometric boundary element method*, Composite Structures, **128**, 54–69.
2. Bazilevs Y., Calo V., Hughes T.J.R., Zhang Y.J. (2008), *Isogeometric fluid-structure interaction: Theory, algorithms, and computations*, Computational Mechanics, **43**, 1, 3–37.
3. Bordas S., Lian H.J., Simpson R. (2013), *Stress analysis without meshing: Isogeometric boundary-element method*, Engineering and Computational Mechanics, **166**, 88–99.
4. Buffa A., Sangalli G., Vazquez R. (2014), *Isogeometric methods for computational electromagnetics: B-spline and T-spline discretizations*, Journal of Computational Physics, **257**, 1291–1320.
5. Burton A.J., Miller G.F. (1971), *The application of integral equation methods to the numerical solution of some exterior boundary-value problems*, Proceedings of The Royal Society A: Mathematical, Physical and Engineering Sciences, **323**, 1553, 201–210.

6. Chen L., Zhao W., Liu C., Chen H. (2017a), *2D structural acoustic analysis using the FEM/FMBEM with different coupled element types*, Archives of Acoustics, **42**, 1, 37–48.

7. Chen L., Chen H., Zheng C., Marburg S. (2016a), *Structural-acoustic sensitivity analysis of radiated sound power using a finite element/ discontinuous fast multipole boundary element scheme: Radiated sound power sensitivity*, International Journal for Numerical Methods in Fluids, **82**, 12, 858–878.

8. Chen L., Liu L., Zhao W., Chen H. (2016b), *2D acoustic design sensitivity analysis based on adjoint variable method using different types of boundary elements*, Acoustics Australia, **44**, 343–357.

9. Chen L., Marburg S., Chen H., Zhang H., Gao H. (2017b), *An adjoint operator approach for sensitivity analysis of radiated sound power in fully coupled structural-acoustic systems*, Journal of Computational Acoustics, **25**, 01, 1750003.

10. Chen L., Liu C., Zhao W., Liu L. (2018), *An isogeometric approach of two dimensional acoustic design sensitivity analysis and topology optimization analysis for absorbing material distribution*, Computer Methods in Applied Mechanics and Engineering, **336**, 507–532.

11. Cho S., Ha S. (2009), *Isogeometric shape design optimization: exact geometry and enhanced sensitivity*, Structural and Multidisciplinary Optimization, **38**, 1, 53–70.

12. Coifman R.R., Rokhlin V., Wandzura S. (1993), *The fast multipole method for the wave equation: a pedestrian prescription*, IEEE Antennas and Propagation Magazine, **35**, 3, 7–12.

13. Coox L., Atak O., Vandepitte D., Desmet W. (2017), *An isogeometric indirect boundary element method for solving acoustic problems in open-boundary domains*, Computer Methods in Applied Mechanics and Engineering, **316**, 186–208.

14. De Luycker E., Benson D.J., Belytschko T., Bazilevs Y., Hsu M. (2011), *X-FEM in isogeometric analysis for linear fracture mechanics*, International Journal for Numerical Methods in Engineering, **87**, 541–565.

15. do Rêgo Silva J J. (1994), *Acoustic and Elastic Wave Scattering Using Boundary Elements*, Computational Mechanics Publications, Southampton.

16. Guiggiani M., Krishnasamy G., Rudolphi T.J., Rizzo F.J. (1992), *A general algorithm for the numerical solution of hypersingular boundary integral equations*, Journal of Applied Mechanics, **59**, 5, 604–614.

17. Hughes T.J., Cottrell J.A., Bazilevs Y. (2005), *Isogeometric analysis: CAD, finite elements, NURBS, exact geometry and mesh refinement*, Computer Methods in Applied Mechanics and Engineering, **194**, 3941, 4135–4195.

18. Kostas K.V., Ginnis A.I., Politis C.G., Kaklis P.D. (2015), *Ship-hull shape optimization with a T-spline based BEM-isogeometric solver*, Computer Methods in Applied Mechanics and Engineering, **284**, 611–622.

19. Kostas K.V., Ginnis A.I., Politis C.G., Kaklis P.D. (2017), *Shape-optimization of 2D hydrofoils using an Isogeometric BEM solver*, Computer-Aided Design, **82**, 1, 79–87.

20. Kupradze V.D. (1965), *Potential methods in the theory of elasticity*, Jerusalem: Israel Programme for Scientific Translation.

21. Lee S., Yoon M., Cho S. (2017), *Isogeometric topological shape optimization using dual evolution with boundary integral equation and level sets*, Computer-Aided Design, **82**, 88–99.

22. Li K., Qian X. (2011), *Isogeometric analysis and shape optimization via boundary integral*, Computer-Aided Design, **43**, 11, 1427–1437.

23. Lian H., Kerfriden P., Bordas S. (2017), *Shape optimization directly from cad: an isogeometric boundary element approach using T-splines*, Computer Methods in Applied Mechanics and Engineering, **317**, 1–41.

24. Liu Y.J., Nishimura N. (2006), *The fast multipole boundary element method for potential problems*, Engineering Analysis with Boundary Elements, **30**, 5, 371–381.

25. Liu C., Chen L., Zhao W., Chen H. (2017), *Shape optimization of sound barrier using an isogeometric fast multipole boundary element method in two dimensions*, Engineering Analysis with Boundary Elements, **85**, 142–157.

26. Liu Z., Majeed M., Cirak F., Simpson R.N. (2018), *Isogeometric FEM-BEM coupled structural-acoustic analysis of shells using subdivision surfaces*, International Journal for Numerical Methods in Engineering, **113**, 9, 1507–1530.

27. Manh N.D., Evgrafov A., Gersborg A.R., Gravesen J. (2011), *Isogeometric shape optimization of vibrating membranes*, Computer Methods in Applied Mechanics and Engineering, **200**, 1343–1353.

28. Marburg S. (2016), *The Burton and Miller method: unlocking another mystery of its coupling parameter*, Journal of Computational Acoustics, **23**, 01, 1550016.

29. Marburg S., Amini S. (2005), *Cat's eye radiation with boundary elements: comparative study on treatment of irregular frequencies*, Journal of Computational Acoustics, **13**, 01, 21–45.

30. Marburg S., Schneider S. (2003), *Influence of element types on numeric error for acoustic boundary elements*, Journal of Computational Acoustics, **11**, 03, 363–386.

31. Marussig B., Zechner J., Beer G., Fries T. (2003), *Fast isogeometric boundary element method based on independent field approximation*, Computer Methods in Applied Mechanics and Engineering, **284**, 458–488.

32. Matsumoto T., Tanaka M., Yamada Y. (1995), *Design sensitivity analysis of steady-state acoustic problems using boundary integral equation formulation*, Jsme International Journal Series C-mechanical Systems Machine Elements and Manufacturing, **38**, 1, 9–16.

33. Merz S., Kessissoglou N., Kinns R., Marburg S. (2010), *Minimisation of the sound power radiated by a submarine through optimisation of its resonance changer*, Journal of Sound and Vibration, **329**, 8, 980–993.

34. Nagy A.P., Abdalla M.M., Gurdal Z. (2010), *Isogeometric sizing and shape optimisation of beam structures*, Computer Methods in Applied Mechanics and Engineering, **199**, 1216–1230.

35. Nguyen B.H., Tran H.D., Anitescu C., Zhuang X., Rabczuk T. (2016), *An isogeometric symmetric Galerkin boundary element method for two-dimensional crack problems*, Computer Methods in Applied Mechanics and Engineering, **306**, 252–275.

36. Peake M.J., Trevelyan J., Coates G. (2013), *Extended isogeometric boundary element method (XIBEM) for two-dimensional Helmholtz problems*, Computer Methods in Applied Mechanics and Engineering, **259**, 93–102.

37. Peake M.J., Trevelyan J., Coates G. (2015), *Extended isogeometric boundary element method (XIBEM) for three-dimensional medium-wave acoustic scattering problems*, Computer Methods in Applied Mechanics and Engineering, **284**, 762–780.

38. Peng X., Atroshchenko E., Kerfriden P., Bordas S. (2017a), *Isogeometric boundary element methods for three dimensional static fracture and fatigue crack growth*, Computer Methods in Applied Mechanics and Engineering, **316**, 151–185.

39. Peng X., Atroshchenko E., Kerfriden P., Bordas S. (2017b), *Linear elastic fracture simulation directly from CAD: 2D NURBS-based implementation and role of tip enrichment*, International Journal of Fracture, **204**, 1, 55–78.

40. Peters H., Kinns R., Kessissoglou N. (2014), *Effects of internal mass distribution and its isolation on the acoustic characteristics of a submerged hull*, Journal of Sound and Vibration, **333**, 6, 1684–1697.

41. Rokhlin V. (1990), *Rapid solution of integral equations of scattering theory in two dimensions*, Journal of Computational Physics, **86**, 2, 414–439.

42. Schenck H.A. (1968), *Improved integral formulation for acoustic radiation problems*, Journal of Acoustic Society of America, **44**, 41–58.

43. Scott M.A. *et al.* (2013), *Isogeometric boundary element analysis using unstructured T-splines*, Computer Methods in Applied Mechanics and Engineering, **254**, 197–221.

44. Simpson R.N., Bordas S., Lian H., Trevelyan J. (2013), *An isogeometric boundary element method for elastostatic analysis: 2D implementation aspects*, Computers & Structures, **118**, 2–12.

45. Simpson R.N., Liu Z. (2016), *Acceleration of isogeometric boundary element analysis through a black-box fast multipole method*, Engineering Analysis with Boundary Elements, **66**, 168–182.

46. Simpson R.N., Scott M.A., Taus M., Thomas D.C., Lian H. (2014), *Acoustic isogeometric boundary element analysis*, Computer Methods in Applied Mechanics and Engineering, **269**, 265–290.

47. Takahashi T., Matsumoto T. (2012), *An application of fast multipole method to isogeometric boundary element method for Laplace equation in two dimensions*, Engineering Analysis With Boundary Elements, **36**, 12, 1766–1775.

48. Taus M., Rodin G.J., Hughes T.J. (2016), *Isogeometric analysis of boundary integral equations: High-order collocation methods for the singular and hypersingular equations*, Mathematical Models and Methods in Applied Sciences, **26**, 08, 1447–1480.

49. Wall W.A., Frenzel M., Cyron C.J. (2008), *Isogeometric structural shape optimization*, Computer Methods in Applied Mechanics and Engineering, **197**, 2976–2988.

50. Wolf W., Lele S.K. (2011), *Wideband fast multipole boundary element method: Application to acoustic scattering from aerodynamic bodies*, International Journal for Numerical Methods in Fluids, **67**, 12, 2108–2129.

51. Zhao W., Chen L., Chen H., Marburg S. (2019), *Topology optimization of exterior acoustic-structure interaction systems using the coupled FEM-BEM method*, International Journal for Numerical Methods in Engineering, **59**, 59, 1–28.

52. Zheng C., Chen H., Gao H., Du L. (2015), *Is the Burton-Miller formulation really free of fictitious eigenfrequencies?*, Engineering Analysis with Boundary Elements, **59**, 59, 43–51.

53. Zheng C., Matsumoto T., Takahashi T., Chen H. (2012), *A wideband fast multipole boundary element method for three dimensional acoustic shape sensitivity analysis based on direct differentiation method*, Engineering Analysis with Boundary Elements, **36**, 3, 361–371.

54. Zieniuk E. (2003), *Bézier curves in the modification of boundary integral equations (BIE) for potential boundary-values problems*, International Journal of Solids and Structures, **40**, 9, 2301–2320.

55. Zieniuk E., Szerszen K. (2014), *The PIES for solving 3D potential problems with domains bounded by rectangular Bézier patches*, Engineering Computations, **31**, 4, 791–809.